Journal of the Southeastern Association for Research in Astronomy, **4**, 15-19, 2010 July 1

MODELING ASYMMETRIC FORBIDDEN LINE EMISSION PROFILES IN SUPERNOVAE WITH CLUMPING

Jessica Herrington,[1]
Department of Physics and Astronomy, Clemson University Clemson, SC 29634

Richard Ignace & K. Tabetha Hole
Department of Physics and Astronomy, East Tennesse State University Johnson City, TN 37614

ABSTRACT

There are some supernovae that display emission line profiles that are asymmetric in shape. One cause for asymmetry could be an in-homogeneous density distribution, or "clumps". We explore the effects of clumps on the emission line profiles of forbidden lines. Our model assumes the ejecta shell is spherically symmetric in velocity, with a central cavity. The model assigns density perturbations to conical sections in the ejecta. To model the emission profile for a forbidden line, we use Sobolev theory. Our model gives asymmetric profiles when the clumping is introduced. The amount of asymmetry varies with the range of density perturbations allowed, and the relative asymmetry evolves in time.

Subject headings: line: profiles—supernovae: core-collapse

1. INTRODUCTION

A core-collapse supernova occurs when the core of a massive star ($M_\star \geq 8M_\odot$) collapses at the end of the star's life (Woosley & Janka 2005). Supernovae (SNe) are divided into several subgroups based on the strength of the H and He lines in their spectra. Type II SNe have both H and He, Type Ib have just He, and Type Ic have neither H nor He in their spectra (for a review, see Filippenko 1997). Type Ia SNe have Si lines in their spectra, and they result from an entirely different mechanism than the previously mentioned types.

It is possible to infer the geometry of the SN ejecta from the shape of the emission lines profiles in the spectra (Mazzali et al. 2007; Taubenberger et al 2009). In particular, forbidden lines are used to probe the shape of SNe ejecta. If the SN ejecta is spherically symmetric, the emission line profile will be symmetric and Gaussian-like when the SN is in the nebular phase. Many SN spectra show this. However, there are several SNe whose spectra show double peaked profiles or asymmetric profiles (Tanaka et al. 2009a). Of particular interest are the asymmetric profiles. These can be caused by large scale clumping in the ejecta material, a massive blob, or a unipolar jet (Taubenberger et al. 2009).

In this paper, we explore asymmetric emission line profiles due to large scale clumping in the ejecta. Section 2 presents an overview of forbidden line formation. Section 3 details the parameters used in our model such as the ejecta shell shape, the type of clumps introduced, and optical depth effects. In Section 4, concluding remarks and future plans are given.

2. FORBIDDEN LINE FORMATION

We present the theory of forbidden line emission that generally follows Osterbrock (1989) regarding the atomic physics and Ignace & Brimeyer (2006) for notation.

We adopt a 2-level approximation for a fine structure transition of an ion species for simplicity with the lower level as '1' and the upper level as '2'. This approximation can work well even for ions with more than two levels (see Appendix B of Ignace & Brimeyer 2006). In regions of high density, de-excitations are dominated by collisions. When the density becomes low enough, de-excitations are dominated by spontaneous decay. This transition from collision dominated de-excitations to those dominated by spontaneous decay occurs at the critical density, n_c. The critical density is defined as

$$n_c = \frac{A_{21}}{q_{21}}, \tag{1}$$

where A_{21} (s^{-1}) is the Einstein A-value for the transition and q_{21} ($cm^3\ s^{-1}$) is the downward volume collisional de-excitation rate. The volume emissivity j_ν (erg s^{-1} cm^{-3} sr^{-1}) is given by

$$j_\nu = \frac{1}{4\pi} h\nu_{21} A_{21} n_2, \tag{2}$$

where h is Planck's constant and n_2 is the second level population density. To determine n_2, we use the following rate expression that governs the equilibrium conditions for the two levels:

$$n_1 n_e q_{12} = n_2 n_e q_{21} + n_2 A_{21}. \tag{3}$$

After some manipulation of the above equations, the equation for volume emissivity becomes

$$j_\nu = j_0 \frac{n_e/n_c}{a + bn_c/n_e} \tag{4}$$

where j_0, a, and b are constants that depend on the ion transition and SN ejecta shell properties (e.g., see Table 1 of Ignace et al. 2009). When $n_e \gg n_c$, the emissivity

Electronic address: herrin4@clemson.edu; ignace@etsu.edu; kthole@etsu.edu
[1] Southeastern Association for Research in Astronomy (SARA) NSF-REU Summer Intern

is proportional to the density, and when $n_e \ll n_c$, the emissivity is proportional to the density squared.

To model emission line profiles, it is necessary to calculate the flux of line emission for the forbidden line as a function of Doppler shift. It is also useful to consider the total line flux. In the case of an optically thin line, the total flux is given by a volume integral over the emissivity (Mihalas 1978):

$$F_\nu = \frac{1}{D^2} \int j_\nu(r)\, dV. \tag{5}$$

where the value D represents the distance from the source of the line emission to the observer.

3. SUPERNOVA EJECTA SHELLS

Asphericity will be introduced as a density fluctuation around a subshell of radius r. However, we assume the ejecta is spherical in geometry and velocity with an inner radius r_1 and an outer radius r_2. The ejecta lies between the two radii, with an empty cavity at $r < r_1$. In the case of spherical symmetry and with the radius bounds given above, Equation 5 becomes

$$F_\nu = \frac{4\pi}{D^2} \int_{r_1}^{r_2} r^2 j_\nu(r)\, dr. \tag{6}$$

Each subshell expands linearly such that $v(r) \propto r$. We introduce a new variable, w, that represents the normalized radial expansion velocity such that $w(r_2) = 1$. The normalized velocity at any subshell becomes,

$$w(r) = \frac{r}{r_2}. \tag{7}$$

The normalized line of sight Doppler shifted velocity is represented as w_z. Assuming the observer to be on the negative z-axis (see Figure 3), w_z is given by

$$w_z = w(r)\cos(\theta). \tag{8}$$

Each subshell within the SN ejecta will have a range of w_z such that $|w_z| \leq w(r)$.

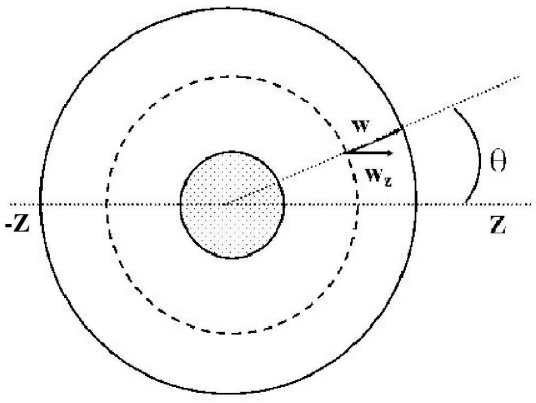

FIG. 1.— This figure shows the schematic for the SN with the observer located at $-\infty$. The dashed circle represents a subshell of radius, r, within the ejecta.

When the density is constant around a subshell, the emissivity is constant, and the amount of flux contributed from each w_z in the subshell is the same. This leads to a flat top emission profile for each subshell (e.g., see Ignace & Hendry 2000). As r decreases, the flat top emission profile from that subshell is smaller in width because $|w_z| \leq w(r)$. Adding up contributions from each subshell, the resultant emission profile is symmetric about $w_z = 0$.

SNe generally have a density structure that follows $\rho \propto r^{-n}$ with $7 < n < 10$ (Arnett 1996). For our exploration, we adopt $n = 8$ for the density power law. The ejecta radii are growing linearly with time, t, as the coasting expansion proceeds, so the volume of the ejecta grows as t^3. Therefore, the local density decreases everywhere like t^{-3}.

As Taubenberger et al. (2009) found in their survey, many SNe have asymmetric emission line profiles. If the ejecta geometry is axisymmetric, such as a disk or two polar jets, the emission profiles should still be symmetric about $w_z = 0$, assuming no continuum absorption. Instead of being Gaussian, these profiles will typically be double peaked. The asymmetric profiles observed are not double peaked, but rather multi-peaked.

To explore profile asymmetry arising from non-symmetric SN explosions, we introduce clumping into our model. We assume the SN ejecta to have a constant clumping perturbation factor with radius, creating conical "wedges" of constant density perturbation in the model. The ejecta is axisymmetric about the z-axis, so these wedges represent cones of constant density perturbation. We introduce a new variable, A_{wedge}, which represents the density perturbation in each conical wedge section. The density per wedge (n_{wedge}) is then

$$n_{wedge} = A_{wedge} n_e(r). \tag{9}$$

Depending on how many wedges there are, the emission line profile can have many subdued peaks (a lot of wedges) or can have a few dominant peaks (fewer wedges).

As Li & McCray (1992) have shown, SNe ejecta can be optically thick in some forbidden lines up to a year after the outburst. Following Li & McCray, we introduce a parameter $P_{\rm esc}$ which represents the probability that a line photon will escape from a given volume. According to Sobolev theory (Mihalas 1978), this value is given by

$$P_{\rm esc}(\tau_L) = \frac{1 - e^{-\tau_L}}{\tau_L}, \tag{10}$$

where τ_L is the line optical depth. We assume $\tau_L \propto n_1 \propto n_e$. With this new factor, Equation 4 becomes

$$j_\nu = j_0 \frac{n_e/n_c}{a + b n_c/n_e} P_{\rm esc}. \tag{11}$$

Figure 3 shows how the total flux of the emission line profile changes over time with varying degrees of optical thickness in the line. The variable $\tau_{L,year}$ represents the value of the line optical depth at r_2 at one year after the outburst. In each panel shown in Figure 3 the ejecta began with $\tau_L \gg 1$ at log(t)=1. The open circles show the results of our model and the dashed and dotted lines show the power law trends for the different segments of the evolution. There are several trends worth mentioning in the panels of Figure 3. We will list them as "Cases" below. Cases 1-4 are summarized in Table 1

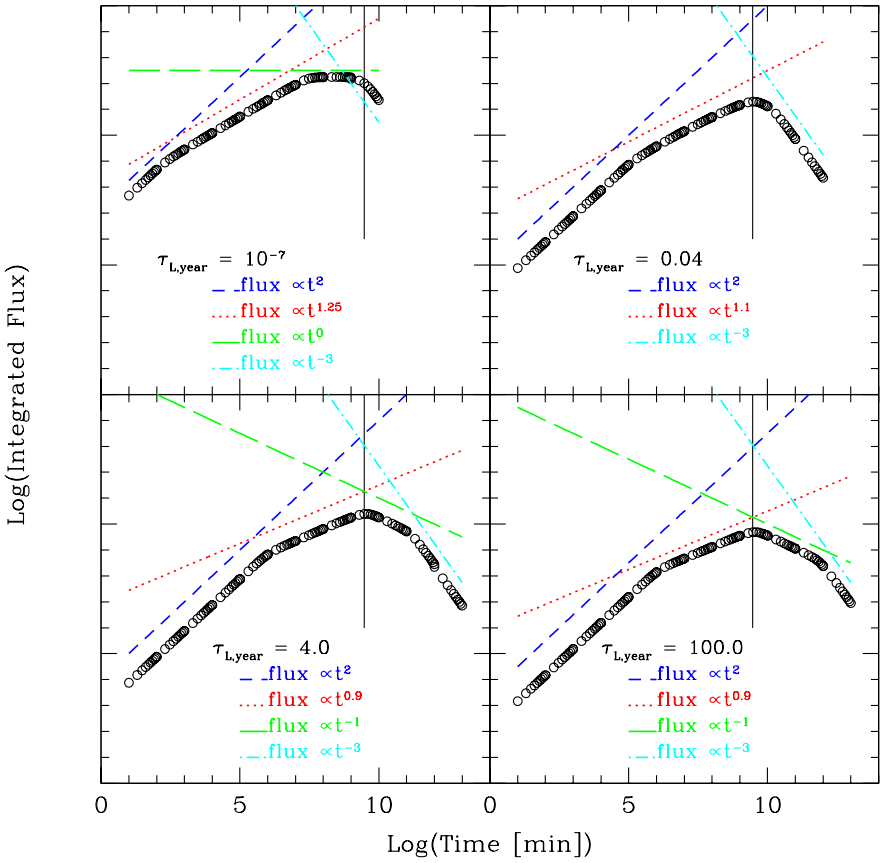

FIG. 2.— These plots shows the trends found for total flux with different τ_L. The various dashed lines show the power law for each segment of the curve. The vertical line represents the time at which all of the ejecta is at a density below the critical density.

TABLE 1
TRENDS IN THE TOTAL FLUX

Case	Thick/Thin[a]	Ejecta Density	Area	Volume	$S_\nu^b \propto$	$j_\nu^c \propto$	$F_\nu \propto$
1	Thick	$n_e > n_c$	t^2	–	t^0	–	t^2
2	Thin	$n_e > n_c$	–	t^3	–	t^{-3}	t^0
3	Thick	$n_e < n_c$	t^2	–	t^{-3}	–	t^{-1}
4	Thin	$n_e < n_c$	–	t^3	–	t^{-6}	t^{-3}

[a] That is $\tau_L >> 1$ or $\tau_L << 1$ respectively
[b] $S_\nu = j_\nu\ (\kappa_\nu \rho)$ where $\kappa\rho \propto n_e$
[c] $j_\nu \propto n_e$ when $n_e > n_c$ and $\propto n_e^2$ when $n_e < n_c$

where the Column 1 is the case number that corresponds with the numbered list below. The second column describes whether the ejecta is optically thick or thin. The third column describes whether the ejecta is above or below the critical density. Columns 4-7 describe how the appropriate variables for the various scenarios described in columns 2 and 3 change with time. The last column gives the overall time dependence of the total flux, F_ν.

1. It is shown in Figure 3 that when $\tau_L \gg 1$ and $n_e > n_c$ throughout all of the ejecta, the flux grows like t^2. When the line is optically thick, $F_\nu \propto S_\nu \times area$, where $S_\nu = j_\nu/(\kappa_\nu\rho)$ with $\kappa_\nu\rho \propto n_e$. The area grows like t^2, while the source function, S_ν, when $n_e > n_c$, is a constant because $j_\nu \propto n_e$. Therefore, $F_\nu \propto t^2$ at early times. This trend is shown by the blue dashed line in all four panels.

2. If all of the ejecta becomes optically thin in the line before $n_e < n_c$, the flux will be constant with time. When the line is optically thin, $F_\nu \propto j_\nu \times volume$. The volume grows like t^3, while the emissivity, j_ν drops as t^{-3} because $j_\nu \propto n_e$ when $n_e > n_c$. Therefore, $F_\nu \propto t^0$. This trend is shown by the green long-dashed line in the top left panel.

3. Once $n_e < n_c$ holds throughout the ejecta, the flux begins to decrease. If some of the ejecta is still optically thick in the line, the flux drops like t^{-1} because S_ν is now proportional to t^{-3} (since $j_\nu \propto n_e^2$ when $n_e < n_c$) while $area \propto t^2$. So, $F_\nu \propto t^{-1}$.

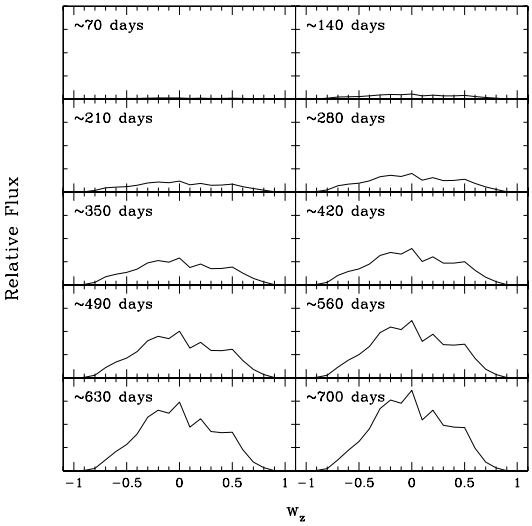

FIG. 3.— Our model of the evolution of a forbidden line profile with clumping, $\tau_L = 0.4$ at r_2 a year after the outburst, and $n_e > n_c$ for each of the 10 plots. Each plot has the same flux scale.

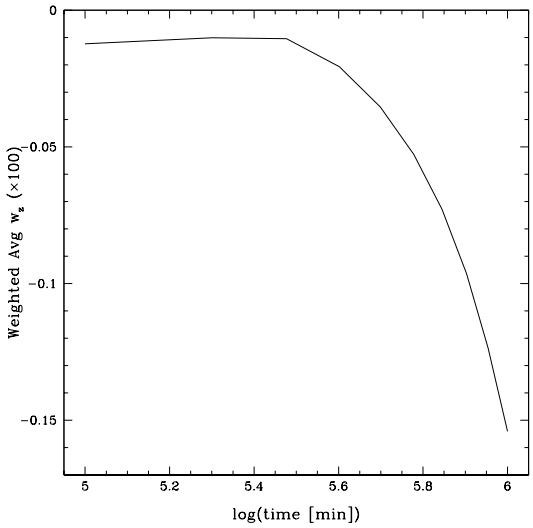

FIG. 4.— This figure shows how the weighted average w evolves over the portion of time shown in Figure 4.

This trend is shown by the green long-dashed line in the bottom left and bottom right panels.

4. When all of the ejecta is optically thin in the line and has a density below n_c, the flux drops like t^{-3} because $j_\nu \propto t^{-6}$ (since $j_\nu \propto n_e^2$ when $n_e < n_c$). Thus, $F_\nu \propto t^{-3}$. This trend is shown by the cyan dashed-dotted line in all four panels.

There is a special case when part (not all) of the ejecta is optically thick in the line while $n_e > n_c$. The power law in this case, represented by the red dotted line, is not the same in each panel. The flux power law depends on what time part of the ejecta becomes optically thin. If this is at very early times, the power law is much higher. As this time becomes later, the power law flattens.

4. MODEL RESULTS

For illustration, we show results for a model with 20 wedges of varying density perturbation, A_{wedge}. A_{wedge} values vary from 1.25 to 0.75. These values are chosen randomly from a uniform distribution in this range. We assume the optical depth in the line to be 0.4 at r_2 at one year after the outburst. Figure 4 shows our model profiles as they evolve from $\sim$ 70 days to $\sim$ 700 days after the outburst. The flux is increasing with each time step because $n_e > n_c$ at these times.

There is asymmetry in the profiles due to the clumping. This asymmetry can be seen by calculation the weighted average of w_z. This value is the w_z value of the peak in the emission profile. In the spherically symmetric case, this peak always lies at $w_z = 0$ when the SN is in the nebular phase. Figure 4 shows the evolution of the weighted average of w_z for Figure 4. The peak in the profile with clumping is not at $w_z = 0$, showing that clumping causes asymmetry.

Figure 4 shows the statistics of the weighted average w_z value over a large span of time for a hundred runs of the model. The mean of the hundred runs is approximately zero. This shows that the peak of the profile is equally likely to lie on either the positive or negative w_z side. For

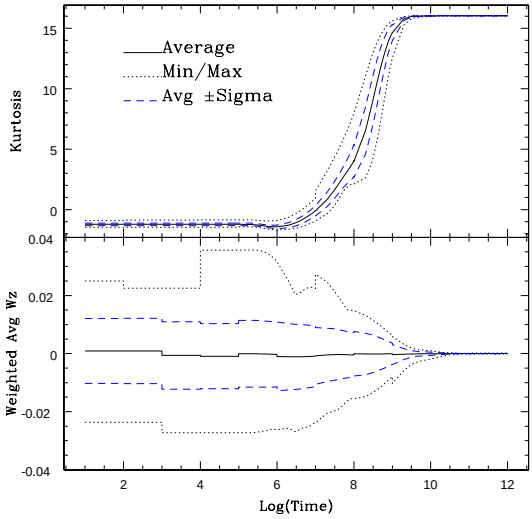

FIG. 5.— This shows the statistics of the weighted average w_z and the kurtosis over 100 runs of our model. The solid black line represents the mean, the dotted black line represents the minimum and maximum values obtained, and the area in between the two dashed blue lines represents where two-thirds of the points lay.

the given density perturbation range above, the peak of the profile is likely to lie within $0.01 v_{max}$ (v_{max} is the maximum Doppler shifted velocity of the profile), or as far as $0.03 v_{max}$ from $w_z = 0$. This range depends on the density perturbation range. If the density perturbations in the wedges span a much larger range, the profile peak is more likely to shift farther away from $w_z = 0$.

The weighted average w_z value tends towards zero at late times. This is due to the nature of the profile shape at later times. The profiles are narrower because the density is decreasing everywhere and emission lines are only coming from the central radii of the ejecta. This causes the profile to be centered on $w_z = 0$ because it is so narrow. We see that the profiles narrow by looking at the kurtosis at late times. A higher kurtosis indicates a profile that has a sharp, narrow peak, relative to a Gaussian

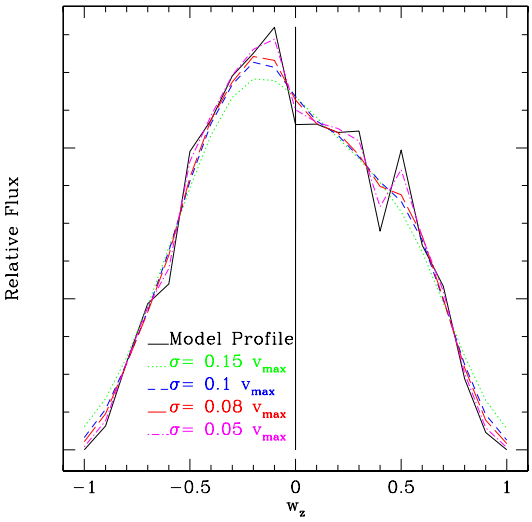

FIG. 6.— This shows a model forbidden line emission profile at ∼ 70 days after the ourburst and several Gaussian smoothed profiles at different resolutions. The model profile has velocity bin spacing of $0.1v_{max}$.

curve. As seen in Figure 4, the kurtosis is higher at late times as compared to earlier times. An interesting result from the kurtosis plot is the section where the kurtosis increases. This occurs when the ejecta is transitioning from $n_e > n_c$ to $n_e < n_c$. When all of the ejecta is either above or below the critical density, the kurtosis is constant.

Our model has shown that clumping of SN ejecta does lead to asymmetric profiles. However, this information cannot be used if the asymmetry cannot be resolved in an observed spectrum. To determine how much asymmetry can be resolved, we Gaussian smoothed a model profile to different resolutions (see Figure 6). We found that at a resolution of $\sim 0.1v_{max}$ the asymmetry is detectable. For $v_{max} = 10,000$ km/s, this is a resolution of about 1000 km/s which is easily achievable, even for low resolution spectragraphs. As the resolution increases, the individual peaks in the profile can be seen.

5. CONCLUSIONS

There are SNe that have been found to have asymmetric emission line profiles. There are several conditions that can cause asymmetric profiles. In this paper we have explored the possibility that clumping within the ejecta is causing this asymmetry. We assumed the ejecta had the same radial clumping factor, causing the ejecta to have conical wedge sections of constant density perturbation. The ejecta shell was allowed to be optically thick in the line up to a year after the outburst. Our model proved that clumping does cause asymmetric profiles, and this asymmetry should be resolvable in an observed spectrum.

The clumping structure used so far would not show polarization in the ejecta because it is symmetric around the line of sight. Observations show that SNe can often be polarized as well as show asymmetry in their emission line profiles (Tanaka et al. 2009b). In the future, we would like to change the clumping structure so our model produces asymmetric forbidden line profiles as well as showing polarization. We would also like to model a doublet profile. This would require proper treatment for the radiative transfer of line blends along with multi-level populations of an atom.

This project was funded by a partnership between the National Science Foundation (NSF AST-0552798), Research Experiences for Undergraduates (REU), and the Department of Defense (DoD) ASSURE (Awards to Stimulate and Support Undergraduate Research Experiences) programs.

REFERENCES

Arnett, D. 1996, Supernovae and Nucleosynthesis: An Investigation of the History of Matter, from the Big Bang to the Present, by D. Arnett. (Princeton, NJ: Princeton University Press)
Filippenko, A. V. 1997, ARA&A, 35, 309
Ignace, R., Bessey, R., & Price, C. S. 2009, MNRAS, 395, 962
Ignace, R., & Brimeyer, A. 2006, MNRAS, 371, 343
Ignace, R., & Hendry, M. A. 2000, ApJ, 537, L131
Li, H., & McCray, R. 1992, ApJ, 387, 309
Mazzali, P. A., et al. 2007, ApJ, 670, 592
Mihalas, D. 1978, Stellar Atmospheres (2nd Ed.;, San Francisco, CA: W. H. Freeman and Co.)
Osterbrock, D. E. 1989, Astrophysics of Gaseous Nebulae and Active Galactic Nuclei, (Mill Valley, CA: University Science Books)
Tanaka, M., et al. 2009a, ApJ, 700, 1680
Tanaka, M., et al. 2009b, ApJ, 699, 1119
Taubenberger, S., et al. 2009, MNRAS, 397, 677
Woosley, S., & Janka, T. 2005, Nature Physics, 1, 147